Simulating DIC Microscope Images: From Physical Principles to a Computational Model.

Farhana Kagalwala

Robotics Institute
Carnegie Mellon University
Pittsburgh, PA 15213
farhana@cs.cmu.edu

Takeo Kanade

Robotics Institute
Carnegie Mellon University
Pittsburgh, PA 15213

Abstract

Differential Interference Contrast (DIC) microscopy is a powerful visualization tool to study live biological cells. Its use in quantitative analysis, however, is limited by the nonlinear relation between image and object. Combining concepts from graphics and physics, we model these nonlinearities using a generalized ray tracer. We verify our model by comparing real image data of manufactured specimens to simulated images of virtual objects. We plan to use this model to iteratively reconstruct the three-dimensional properties of unknown specimens.

1 Introduction

The Nomarski Differential Interference Contrast (DIC) microscope is the preferred method for visualizing live biological specimens. To date, biologists only qualitatively investigate images of live cell specimens taken via the DIC microscope. The nonlinear relationship between image and object has hindered past attempts at quantitative analysis. In this paper, we describe a computational model of the DIC imaging process. The model is the first step in reconstructing properties of the specimen, viewed under the DIC microscope, quantitatively.

DIC microscopy offers several advantages over brightfield, fluorescence and confocal microscopes. Since the DIC microscope is an interferometer, live, transparent specimens can be examined with it. Due to higher axial resolution, three-dimensional objects are better resolved. No dyes, which may harm live specimens, are injected. Finally, an optically-sectioned set of images can be acquired under a minute, which offers adequate time-sampling for live metamorphosing cells.

Looking through the eyepiece, an observer sees the differential of the optical path length introduced by the object into the propagating light wave. The differential is along a transverse direction, called the shear direction. Example DIC images are shown in Figure 1. In the microscope, shown in Figure 2, an incident, polarized light wave is sheared into two wavefronts by a birefringent prism. The wavefronts propagate a differential distance apart through the specimen. The im-

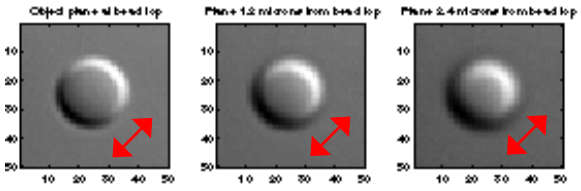

Figure 1: Example DIC Image of Bead: The specimen contained a 10μm polystyrene bead embedded in optical cement, with refractive index difference of .03. The leftmost image has the bead in focus while in the other two images the bead is increasingly de-focused. The arrow indicates the shear direction.

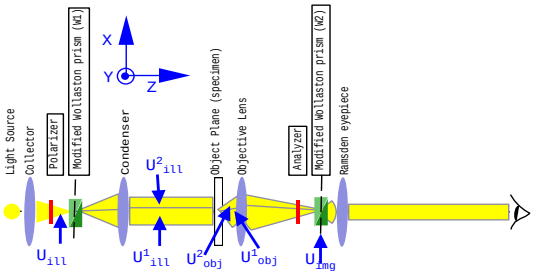

Figure 2: DIC Optical Components: The boxed labels identify components that are absent in a regular brightfield microscope. The dashed lines indicate virtual planes of reference. The labels denoted with "U" are explained in the text.

age intensity is the interference pattern due to their superposition.

Theoretically, the DIC imaging process can be understood by first considering a wavefront, represented by

$$U_{ill}(\vec{x}) = A\exp[-i\phi_{ill}(\vec{x})]. \quad (1)$$

where $\vec{x} = (x, y, z)$ denotes the coordinate space of the object with the z-axis parallel to the optical axis. The two sheared wavefronts resulting from the Nomarski prisms, $U^1_{ill}(\vec{x})$ and $U^2_{ill}(\vec{x})$, are

$$U^1_{ill}(\vec{x}) = A\exp[-i[\phi_{ill}(\vec{x}+\vec{v}_s) + \Delta\phi_{bias}]] \quad (2)$$

$$U^2_{ill}(\vec{x}) = A\exp[-i\phi_{ill}(\vec{x}-\vec{v}_s)] \quad (3)$$

where $2\vec{v}_s$ is the shear vector and $\Delta\phi_{bias}$ is the phase bias. After incorporating the phase transformation introduced by the object, $\phi_{obj}(\vec{x})$, the wavefronts $U^1_{obj}(\vec{x})$ and $U^2_{obj}(\vec{x})$ represent the object information by

$$U^1_{obj}(\vec{x}) = A\exp[-i[\phi_{obj}(\vec{x}+\vec{v_s}) + \Delta\phi_{bias}]] \quad (4)$$

$$U^2_{obj}(\vec{x}) = A\exp[-i\phi_{obj}(\vec{x}-\vec{v_s})]. \quad (5)$$

The amplitude of the field in the image space is

$$U_{img}(\vec{x}_{img}) = \int_{y_0^{obj}}^{y_1^{obj}}\int_{x_0^{obj}}^{x_1^{obj}} K_z(x_{img}, y_{img}, x, y) [U^1_{obj}(x, y, z = z_1) - U^2_{obj}(x, y, z = z_1)]dxdy \quad (6)$$

where $K_z(x_{img}, y_{img}, x, y)$ is the transmission function of the imaging system (objective and any other auxiliary lens) of the microscope. $\vec{x}_{img} = (x_{img}, y_{img}, z_{img})$ represents the coordinate space of the image with the z-axis parallel to the optical axis. $K_z(...)$ describes the propagation from the object plane at $z = z_1$ to the image plane z_{img}. The image intensity is simply $|U_{img}(x_{img}, y_{img}, z_{img})|^2$.

The nonlinearities in the DIC image have two basic sources. First, since the image is an interference pattern, it is linear in the light wave's complex amplitude, not its intensity. In other words, the image intensity is actually the squared magnitude of the linearly superposed complex amplitude components of the light wave, as shown in Equation 6. In addition, out of focus contributions from the object have to be considered, and therefore a three-dimensional amplitude point spread (or transmission) function has to be computed. Second, the object itself aberrates the light wave as it propagates through, and these aberrations contribute significantly to the image.

Our model attempts to address each of the above complications by using a generalized ray tracing method. Based on energy-conservation laws, the paths of light propagation are traced through the object. An aberrated wavefront at the lens plane is approximated and the resulting intensity distribution at the image plane is calculated. We evaluate this model by comparing real and simulated images of actual and virtual three dimensional objects, respectively. This model is currently being used to reconstruct the refractive-index distribution across the specimen volume.

2 Previous Models

Deconvolution methods, such as computational optical sectioning microscopy (COSM) are widely used to reconstruct object information from images of certain modalities. The image intensity, which is three-dimensional, can be modelled as a convolution of the intensity transmittance of the object with a computed point-spread function. In modalities such as fluorescence and brightfield, the image is a linear function of the intensity of the object field, to a good approximation However, in DIC microscopy, the image cannot be accurately represented by an intensity superposition.

One of the earliest models of DIC optics was formulated by Galbraith in 1982[9]. Under assumptions of a thin object, with thickness less than the microscope's depth of field, a complex amplitude point spread function is formulated in the work. A signal-processing model for DIC optics was formulated by Holmes and Levy in 1987[13]. In recent years, Cogswell and Sheppard extended previous models of DIC optics to include partially-coherent illumination [4].

In 1996, Feinegle used a contour finding algorithm to locate edges in each image from an optically-sectioned stack. In this work, each image in the stack was filtered to reveal in-focus features, and therefore some attempt was done to model the object in three-dimensions[7]. The most recent work in the analysis of DIC images has been done by Preza. This work attempts to recover the optical pathlength at each image point due to the object[20]. Though, no attempt is made to reconstruct the three dimensional properties of the object.

3 Computational Model

Our computational model consists of a polarized ray tracer and an approximation of the wave aberrations due to diffraction by the lens and due to the self-occlusion by the object. The model computes the intensity contribution at the image plane dictated by energy conservation laws. Polarization ray tracing methods are used to trace rays through the prisms. The lens, assumed to be an ideal thin lens, and polarizers are handled by a transfer matrix. For details on the prism, lens and polarizers, please refer to a previous paper [15].

3.1 Light Propagation

Using the principles of geometrical optics, a ray tracer simulates the interaction of an impinging light wavefront on an object. Standard rays are linear vectors that represent the intensity propagated along the solid angle around the vector. In our model, this standard model of a ray is generalized.

A time harmonic, monochromatic, polarized electric field can be represented by a vector-valued amplitude and phase. Surfaces of constant phase are called wavefronts. Light rays are defined as the trajectories orthogonal to the wavefronts.

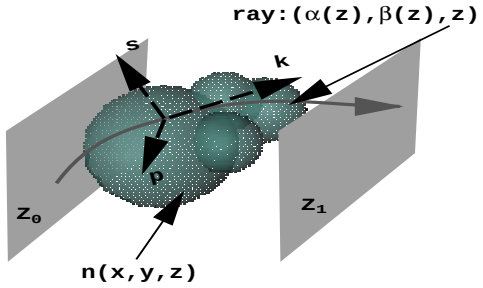

Figure 3: Schematic of a hypothetical ray path: The entrance and exit planes are labelled z_0 and z_1 respectively. The local coordinate system of the ray is labelled as the vectors $\vec{k}$, $\vec{s}$, and $\vec{p}$.

Through an inhomogeneous medium, the light rays are three-dimensional curves, represented by $(\alpha(z), \beta(z), z)$. Let the refractive index distribution of the medium be $n(x, y, z)$ which extends between the z-planes z_0 and z_1. Refer to Figure 3. According to Fermat's principle, $\alpha(z)$ and $\beta(z)$ minimize the following variational integral

$$\int_{z_0}^{z_1} n(\alpha(z), \beta(z), z)\sqrt{\alpha'(z)^2 + \beta'(z)^2 + 1}dz. \quad (7)$$

$\alpha(z)$ and $\beta(z)$ solve a set of initial-valued Euler-Lagrange differential equations. Light rays in our model, are discretely approximated bi-characteristics of these differential equations. The variational method is consistent with the Hamiltonian formulation of energy conservation [2].

For each initial valued point, $x_0 = \alpha(z_0)$ and $y_0 = \beta(z_0)$, the variational problem is solved by a particular curve, $(\alpha_p(z), \beta_p(z), z)$. The intersection of the curve with the $z = z_1$ plane is a point $(x_1 = \alpha_p(z_1), y_1 = \beta_p(z_1), z_1)$. In our model, rays which enter the object at a specific point with a specific angle provide the initial values: $\alpha(z_0), \beta(z_0), \alpha'(z_0), \beta'(z_0)$.

To state the initial-valued system of differential equations, we define,in addition to $\alpha(z)$,$\beta(z)$ and $n(x, y, z)$, the following variables

$$\begin{aligned} n_x &= \frac{\delta n}{\delta x} \\ n_y &= \frac{\delta n}{\delta y} \\ n_z &= \frac{\delta n}{\delta z} \\ w &= \sqrt{\alpha_z^2 + \beta_z^2 + 1}. \end{aligned} \quad (8)$$

The resulting differential equations are

$$\begin{aligned} \frac{d\alpha}{dz} &= \alpha_z \\ \frac{d\beta}{dz} &= \beta_z \\ \frac{d\alpha_z}{dz} &= \frac{w^3}{n(w^2 - \alpha_z)} \times \left[n_x(w - \frac{\alpha_z^2}{w}) - n_z w \right] \\ \frac{d\beta_z}{dz} &= \frac{w^3}{n(w^2 - \beta_z)} \times \left[n_y(w - \frac{\beta_z^2}{w}) - n_z w \right]. \end{aligned} \quad (9)$$

The above equations are integrated using a fourth-order Runge-Kutta method [23]. The value of the integral in Eq. 7 for this particular solution is the optical pathlength from (x_0, y_0, z_0) to (x_1, y_1, z_1). The optical pathlength values at all points on the plane $z = z_1$ defines a function $\psi_{z_1}(x_1, y_1)$ across that plane. The phase transformation, used in Eq. 4, is defined as

$$\phi_{obj}(x, y, z_1) = (2\pi\psi_{z_1}(x, y)/\lambda), \quad (10)$$

where λ is the wavelength of the propagating light.

In our model, each ray contains the local field amplitude polarization, propagation direction, and phase information. The local coordinate system at each ray consists of the propagation vector $\vec{k}$ and two orthogonal vectors, $\vec{s}$ and $\vec{p}$, in the plane perpendicular to $\vec{k}$. The amplitude polarization of the local field is stored with each ray as Jones vectors (described below).

Any field amplitude polarization can be decomposed into two vectors orthogonal to the propagation direction—such as $\vec{s}$ and $\vec{p}$ above. Each vector is weighted by a complex scalar. The scalar coefficients of the polarized electric field, E_s and E_p, are the components of Jones vectors. Therefore,

$$\vec{E} = \begin{bmatrix} E_s \\ E_p \end{bmatrix} = \begin{bmatrix} E_{0s}e^{i\phi_s} \\ E_{0p}e^{i\phi_p} \end{bmatrix} \quad (11)$$

represents the polarization state of a coherent wave.

3.2 Object Model

The specimen model consists of a 3-D grid of voxels. Each voxel contains a refractive index value, labelled as $n_{[i,j,k]}$. Suppose the refractive index distribution through the complete object volume is a continuous function, $n(\vec{x})$. Each voxel contains a uniformly sampled value of $n(\vec{x})$ with the interval size $\Delta\vec{x}$ and $\nabla n(x, y, z)|_{x=i\Delta x, y=j\Delta y, z=k\Delta z}$[1]. To calculate the three dimensional curves, i.e. to solve Eq. 9, we use these discrete values.

3.3 Wave Aberrations

In macroscopic imaging situations with either opaque or transparent objects of a constant refractive index, aberrations due to the object can be largely ignored. Here the most significant aberrations are due to the object's distance from the plane in focus. When imaging microscopic, transparent specimens with variable refractive index distributions, in addition to the

[1] $(\Delta x, \Delta y, \Delta z)$ is the resolution of the voxel grid.

defocusing artifacts, the object itself aberrates the propagating wavefront. These aberrations by the object are significant, as shown in Figure 4, and need to be modelled.

Traditional ray tracing methods implement the defocusing effects by having an explicit object boundary surface from which rays exit. A blurring function is used to distribute the intensity along each ray to multiple pixels. The function's spread is proportional to the distance from the boundary point to the plane in focus. With biological cells, a boundary surface often cannot be defined because the refractive index variations between the cell and its medium are very small and irregular. Therefore, in the case of most cells, the macroscopic notion of boundary is ill-defined. In our model, we compute the aberrations due to the object by considering the wave propagation through the volume, bypassing a surface based approach.

By studying the wavefront reaching the lens from each point in the object, we have approximated the aberration in the wavefront and incorporated it into our model. At sampled points of the object, we trace a solid angle of rays to the entrance plane of the lens, as shown in Figure 5. The maximum angle subtended by the rays is equal to the maximum angle of rays illuminating the object. [2] The point where the axial ray (ray parallel to the optical axis) intersects the lens plane is the center of the wavefront. The axial ray's phase at that point of intersection is the reference phase. The wavefront surface is identified by the locations at which all the other rays in the solid angle have the same phase value. The curvature of this surface is computed by finding the curvature along two orthogonal curves on the wavefront surface and calculating the mean curvature.

A convex lens focuses an impinging wavefront by modifying the curvature of that wavefront as it propagates through the lens. The lens law,

$$\frac{1}{d_i} + \frac{1}{d_o} = \frac{1}{f_l}, \tag{12}$$

where d_i is the distance from the center of the lens to the image plane, d_o is the distance to the object plane from the lens center, and f_l is the focal length of the lens, determines the curvature of the correctly focused wavefront impinging on the lens plane. Therefore any deviation, from ideal, of the impinging wavefront's curvature will result in a spherical aberration. We found by numerous simulations that the objects under study only significantly change the wavefront's curvature. Therefore the aberrations caused by the object can be approximated as defocusing effects. Another way of viewing this is that the object distorts the imaginary plane that would correctly focus onto the image plane as shown in Figure 4.

3.4 Image Formation

The ray tracing step provides the absolute phase from each part of the object, which is the contribution of that object voxel to U_{img} (in Eq. 6). Whereas,

[2] The condenser lens' numerical aperture determines the illuminating angle

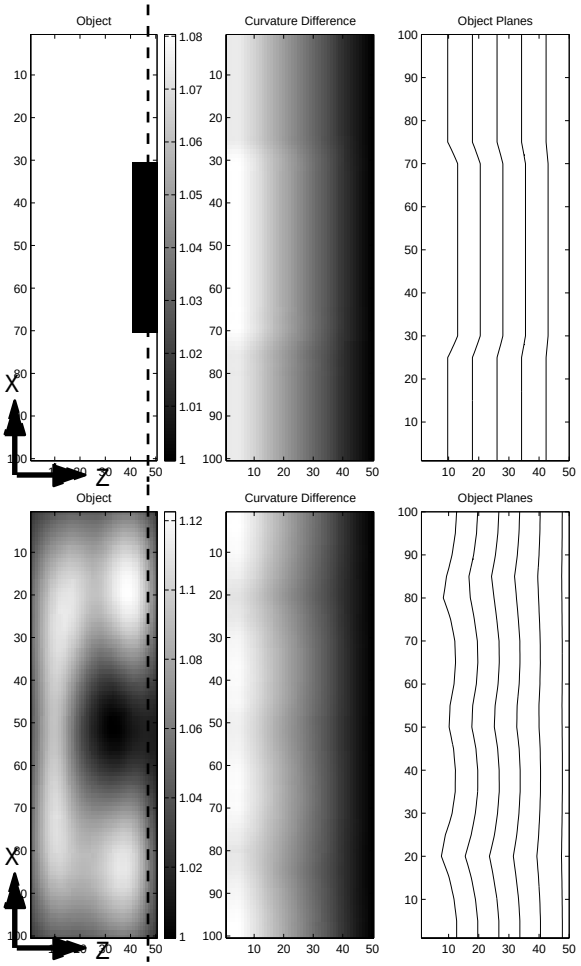

Figure 4: Example objects with corresponding aberrations. In both rows the first column shows a two dimensional object's refractive index distribution, with its scale to the right. The total distance shown is 10 μm in x and 3 μm in z, for each object. The center image in both rows show expected aberrations from each point in the object. The plot actually shows the difference between actual wavefront curvature values and the ideal value if the plane of focus is the dashed line. Black - white indicate small - large differences. The aberrations caused by the depression are significant since the values are on the order of the defocusing aberrations. The last column in each row shows the aberration effects plotted as distorted planes of focus through the object.

rays

object